AIAA JOURNAL
Vol. 40, No. 3, March 2002

Parallel Computation of Forward Radiated Noise of Ducted Fans with Acoustic Treatment

Yusuf Özyörük*
Middle East Technical University, 06531 Ankara, Turkey

Forward radiated noise of ducted fans is computed numerically on parallel processors solving the three-dimensional, time-dependent Euler equations in body-conformed coordinates with a fourth-order-accurate, finite-difference, Runge–Kutta time-integration scheme. Sound attenuation effects of inlet wall acoustic treatment are included in computations employing a time-discrete form of the standard impedance condition. A distributed computing approach with domain decomposition is used for integrating the equations in parallel using the message passing interface library routines. The abilities of the method are demonstrated with hard- and soft-wall simulations of the JT15D inlet, including flow effects.

I. Introduction

INCREASED sizes of turbofan engines have placed more emphasis on fan noise. Reducing this noise relies heavily on acoustic treatment (liners) of the ducting system of the engine. Careful selection of the lining material and its installation require detailed analysis of the sound fields of the engine inlet and exhaust ducts. To date such analysis with liners has been done successfully only in the frequency domain,[1] whereas time-domain studies treated only hard-walled ducts.[2–4] This is because the behavior of lining materials is frequency dependent, and an appropriate boundary condition was not given in the time domain.

A numerical procedure for the application of the classical frequency-dependent impedance condition[5] in the time domain was, however, devised by Özyörük and Long[6] using the z transform, establishing a connection between the frequency and time domains. This technique was utilized for numerical simulations of a flow-impedance tube and was validated by these authors by comparing results with experiment.[7,8] This method is extended in the present paper to curved walls for numerical predictions of noise radiation from lined ducted fans. Solutions are obtained using the full, three-dimensional, time-dependent Euler equations as the governing equations. Nonreflecting conditions are imposed at the far-field boundaries of the finite computational domain. Eigensolutions to the standard cylindrical duct problem are used as an acoustic source at the interface between the fan and inlet region. Acoustic information is extracted by subtracting the mean flowfield from the instantaneous one. These are described in the next section. Then, applications of the method to the JT15D turbofan inlet are demonstrated using plane wave and spinning modes. Results are compared with experiment for the spinning (13, 0) mode.

II. Mathematical Model

A. Governing Equations

The three-dimensional, time-dependent Euler equations in cylindrical coordinates are used as the governing equations. These equations are transformed into a body-fitted curvilinear coordinate system through the mappings $x = x(\xi, \eta, \zeta)$, $r = r(\xi, \eta, \zeta)$, and $\theta = \theta(\xi, \eta, \zeta)$, where x, r, and θ are the cylindrical coordinate directions and ξ, η, and ζ are the curvilinear coordinate directions. Thus, the transformed equations can be written in the form

$$\frac{\partial \tilde{\boldsymbol{Q}}}{\partial t} + \frac{\partial \tilde{\boldsymbol{E}}}{\partial \xi} + \frac{\partial \tilde{\boldsymbol{F}}}{\partial \eta} + \frac{\partial \tilde{\boldsymbol{G}}}{\partial \zeta} + \tilde{\boldsymbol{S}} = 0 \tag{1}$$

where $\tilde{\boldsymbol{Q}} = J^{-1}\boldsymbol{Q}$, $\tilde{\boldsymbol{E}} = J^{-1}(\xi_x \boldsymbol{E} + \xi_r \boldsymbol{F} + r^{-1}\xi_\theta \boldsymbol{G})$, $\tilde{\boldsymbol{F}} = J^{-1}(\eta_x \boldsymbol{E} + \eta_r \boldsymbol{F} + r^{-1}\eta_\theta \boldsymbol{G})$, $\tilde{\boldsymbol{G}} = J^{-1}(\zeta_x \boldsymbol{E} + \zeta_r \boldsymbol{F} + r^{-1}\zeta_\theta \boldsymbol{G})$, and $\tilde{\boldsymbol{S}} = J^{-1}r^{-1}\boldsymbol{S}$, in which J is the Jacobian of the coordinate transformation. $\boldsymbol{Q}$ is the conservative solution vector in cylindrical coordinates, that is, $\boldsymbol{Q} = [\rho, \rho u, \rho v, \rho w, \rho e]^T$, where ρ is the density; u, v, and w are the velocity components in the x, r, and θ directions, respectively; and e is the total energy per unit volume. $\boldsymbol{E}$, $\boldsymbol{F}$, and $\boldsymbol{G}$ are the vector components of the flux tensor, and $\boldsymbol{S}$ is the source vector that arises in cylindrical coordinates. The terms $\boldsymbol{E}$, $\boldsymbol{F}$, $\boldsymbol{G}$, and $\boldsymbol{S}$ may be found in standard textbooks and are not repeated here.

B. Boundary Conditions

1. Far-Field Conditions

Calculations are carried out on a finite computational domain employing nonreflecting boundary conditions on the far-field boundary. The conditions proposed by Tam and Webb[9] and Bayliss and Turkel[10] are used as the nonreflecting conditions. These boundary conditions are put in cylindrical coordinates so that the same mapping transformations as in the interior apply to them.

2. Fan-Face Conditions

The steady part of the solution (mean flow) is obtained using one-dimensional characteristics-based boundary conditions at the fan face. These conditions drive the local variables to some mean values at the fan stage, which are determined a priori based on one-dimensional gasdynamics relations using the mass flow rate (MFR) and freestream Mach number information as the operating conditions.

Exact cylindrical duct eigensolutions are used at the fan face to excite the acoustic field, which is assumed to be a deviation from the mean field. For the cases of no mass flow through the duct, velocity perturbations are specified at the fan face. These perturbations are obtained substituting the exact acoustic pressure expression into the momentum equations. The other dependent variables are obtained from the Euler equations as the interior domain. However, when there is flow through the duct, the acoustic pressure at the fan face is specified, and the Euler equations are solved for the other variables. Although specification of pressure at the fan face is overrestrictive for downstream propagating waves, which may be created by a liner and/or impedance mismatches due to nonuniform duct cross sections, this approach worked sufficiently well for most of the cases discussed in this paper. It was determined that, when the liner induced modes are strong, reflections from the fan-face boundary may occur and in turn contaminate far-field sound, which indicates that the present fan-face conditions must be improved. Implementing more robust, characteristics-based conditions is the subject of current research. The rotor–stator interaction theory of Tyler and Sofrin[11] is employed to determine which modes are created with

Received 29 August 2000; revision received 9 August 2001; accepted for publication 20 August 2001.

*Associate Professor, Department of Aeronautical Engineering; Yusuf@ae.metu.edu.tr.

the local mean-flow conditions. Multiple modes and multiple harmonics of the blade passing frequency (BPF) can be superimposed to form the source.

3. Hard-Wall Conditions

A proper condition for Euler calculations on a hard wall is that the normal velocity vanish. In other words, fluid particles are allowed to slip at a hard wall. Numerically, the normal component of the contravariant velocity, which is given by $V_C = \eta_x u + \eta_r v + (\eta_\theta/r)w$ in this paper with an orthogonal mesh, is set to zero, but the values of the tangential contravariant velocity components, which are given by $U_C = \xi_x u + \xi_r v + (\xi_\theta/r)w$ and $W_C = \zeta_x u + \zeta_r v + (\zeta_\theta/r)w$, are extrapolated from the interior solution. Density is also extrapolated from the interior. Then, when it is assumed that the grid lines are orthogonal at the wall, pressure is found from the normal momentum equation

$$\frac{\partial p}{\partial \eta} = -\frac{\rho V_t^2}{\left[\eta_x^2 + \eta_r^2 + (\eta_\theta/r)^2\right]^{\frac{1}{2}} R} \tag{2}$$

where V_t is the tangential velocity and R is the radius of wall curvature, which may be found using the metrics.

4. Time-Discrete Impedance Condition

An acoustic impedance condition is applied on acoustically treated surfaces (liner). Because of the slip condition at the wall and because there is in general fluid penetration into an acoustic treatment element, that is, nonzero normal velocity exists, the same equations as in the interior are solved for the velocity components, but the energy equation is replaced with the impedance condition equation. The time-discrete form of the impedance condition is given as[7]

$$\left(p_a^{n+1} - p_a^n\right)/\Delta t + \mathcal{L}_0\, p_a^{n+1} = -a_0\left(v_{a,n}^{n+1} - v_{a,n}^n\right)/\Delta t - R_a^n \tag{3}$$

where p_a is the pressure perturbation, superscript n is the time step, Δt is the time increment from one step to the next, $v_{a,n}$ is the normal component of the velocity perturbation, and $\mathcal{L}_0$ is the spatial operator, $\mathcal{L}_0 = \boldsymbol{V}_0 \cdot \nabla - \boldsymbol{n} \cdot (\boldsymbol{n} \cdot \nabla \boldsymbol{V}_0)$, with $\boldsymbol{V}_0$ the mean velocity and $\boldsymbol{n}$ the surface normal. When there is transformation from the frequency domain to the time domain, the effects of the past acoustic field on the current solution are contained in the R_a^n term given by

$$R_a^n = \sum_{\ell=1}^{M_N} a_\ell \left[\frac{v_{a,n}^{n+1-\ell} - v_{a,n}^{n-\ell}}{\Delta t}\right] - \sum_{k=1}^{M_D} b_k \left[\frac{p_a^{n+1-k} - p_a^{n-k}}{\Delta t} + \mathcal{L}_0\, p_a^{n+1-k}\right] \tag{4}$$

where the constant parameters $a_{0,1,\ldots,M_D}$ and $b_{1,\ldots,M_N}$ are related to the z transform of the functional form of the frequency-dependent impedance data.[7]

Implementation of the impedance condition was described previously for two-dimensional problems with flat walls. However, the inlet wall of a turbofan is not flat, and the wall curvature effects must be taken into account properly. This is done in this paper by writing the spatial operator $\mathcal{L}_0$ in the form $\mathcal{L}_0 = U_{0,C}\,\partial/\partial\xi + W_{0,C}\,\partial/\partial\zeta + \nabla\eta \cdot \partial \boldsymbol{V}_0/\partial\eta$, where $U_{0,C}$ and $W_{0,C}$ are the mean tangential contravariant velocity components, respectively. Note that the mean flow satisfies the flow tangency, and hence, the normal contravariant velocity $V_{0,C}$ is zero. The impedance condition and the momentum equations are coupled on curved walls as described in the next section.

C. Numerical Implementation

A four-stage Runge–Kutta time-integration scheme is employed to advance the solution in time. Spatial derivatives are evaluated using fourth-order accurate finite differencing. Because central schemes lack dissipation mechanisms, artificial dissipation is used to suppress the development of spurious waves. The amount of dissipation added is based on the local flow gradients. The stages of the Runge–Kutta (R–K) scheme are given by

$$\boldsymbol{Q}^{(0)} = \boldsymbol{Q}^n, \qquad \boldsymbol{Q}^{(s)} = \boldsymbol{Q}^n - \alpha_s \Delta t J\left[\mathcal{R}\left(\boldsymbol{Q}^{(s-1)}\right) - \mathcal{D}\left(\boldsymbol{Q}^{(0)}\right)\right]$$
$$\boldsymbol{Q}^{n+1} = \boldsymbol{Q}^{(4)}, \qquad \alpha_s = \left[\tfrac{1}{4}, \tfrac{1}{3}, \tfrac{1}{2}, 1\right] \quad \text{for} \quad s = 1, 2, 3, 4 \tag{5}$$

where $\mathcal{R}(\boldsymbol{Q})$ and $\mathcal{D}(\boldsymbol{Q})$ indicate the residual of the governing equations [sum of the spatial derivatives and the source term in Eq. (1)] and dissipation, respectively.

The interior solution scheme and the time-discrete impedance condition are coupled through the linearized normal momentum equation written at the wall, with $\boldsymbol{V} = \boldsymbol{V}_0 + \boldsymbol{V}_a$ being velocity decomposition, as

$$\frac{\partial v_{a,n}}{\partial t} + \mathcal{L}\, v_{a,n} + \mathcal{L}_a\, v_{0,n} - \boldsymbol{V}_0 \cdot \mathcal{L}_a \boldsymbol{n} - \boldsymbol{V}_a \cdot \mathcal{L}\boldsymbol{n} + \frac{1}{\rho_0}\frac{\partial p_a}{\partial n} - \frac{\rho_a}{\rho_0^2}\frac{\partial p_0}{\partial n} = 0 \tag{6}$$

where $v_{0,n}$ is the normal component of the mean velocity, $\mathcal{L} = U_{0,C}\,\partial/\partial\xi + V_{0,C}\,\partial/\partial\eta + W_{0,C}\,\partial/\partial\zeta$, $\mathcal{L}_a$ is the perturbed equivalent of $\mathcal{L}$, ρ_0 is the mean density, and ρ_a is the density perturbation. In curvilinear coordinates, it can be shown that Eq. (6) transforms to

$$\frac{\partial v_{a,n}}{\partial t} + U_{0,C}\frac{\partial v_{a,n}}{\partial \xi} + V_{a,C}\frac{\partial v_{0,n}}{\partial \eta} + W_{0,C}\frac{\partial v_{a,n}}{\partial \zeta} + \frac{2u_{0,\xi}u_{a,\xi}}{R_\xi} + \frac{2w_{0,\zeta}w_{a,\zeta}}{R_\zeta} + \frac{1}{\rho_0}|\nabla\eta|\frac{\partial p_a}{\partial \eta} - \frac{\rho_a}{\rho_0^2}|\nabla\eta|\frac{\partial p_0}{\partial \eta} = 0 \tag{7}$$

where $V_{a,C}$ is the normal component of the contravariant velocity perturbation; $u_{0,\xi}$ and $w_{0,\zeta}$ are the mean tangential velocity components in the ξ and ζ directions, respectively; R_ξ and R_ζ are the radii of wall curvature in the ξ and ζ directions, respectively; and $|\nabla\eta| = [\eta_x^2 + \eta_r^2 + (\eta_\theta/r)^2]^{1/2}$. For most cases the mean flow is axisymmetric; thus, both $W_{0,C}$ and $w_{0,\xi}$ are zero in Eq. (7). When it is assumed that this is the case, the time discretization of the linearized normal momentum equation is given on the impedance wall as follows:

$$\frac{v_{a,n}^{(s)} - v_{a,n}^n}{\alpha_s \Delta t} + U_{0,C}\frac{\partial v_{a,n}^n}{\partial \xi} + |\nabla\eta|\left[v_{a,n}^{(s)}\frac{\partial v_{0,n}}{\partial \eta} + \frac{1}{\rho_0}\frac{\partial p_a^{(s)}}{\partial \eta} - \frac{\rho_a^{(s)}}{\rho_0^2}\frac{\partial p_0}{\partial \eta}\right] + \frac{2u_{0,\xi}u_{a,\xi}^{(s)}}{R_\xi} = 0 \tag{8}$$

We evaluate some of the terms at the R–K stage s for enhancing stability.[7] The tangential velocity perturbation $u_{a,\xi}$ and the density perturbation ρ_a are extrapolated from the interior solution once they are available from integration of the interior equations. Then this equation is substituted for the time derivative of the normal velocity perturbation into the impedance condition rewritten for an R–K stage s in the form

$$\frac{p_a^{(s)} - p_a^n}{\alpha_s \Delta t} + \mathcal{L}_0\, p_a^{(s)} = \frac{-a_0\left(v_{a,n}^{(s)} - v_{a,n}^n\right)}{\alpha_s \Delta t} - R_a^n \tag{9}$$

After rearrangement and discretization of the resulting equation, the following form of linear system of equations can be obtained for the pressure perturbations at wall mesh points indexed by subscript pair i, k:

$$g_{i,k}\, p_{i-2,k}^{(s)} + h_{i,k}\, p_{i-1,k}^{(s)} + d_{i,k}\, p_{i,k}^{(s)} + e_{i,k}\, p_{i+1,k}^{(s)} + f_{i,k}\, p_{i+2,k}^{(s)} = \mathrm{RHS}_{i,k} \tag{10}$$

where the right-hand side is RHS and the acoustic pressure is given by p to avoid a crowd of subscripts. This system of equations is solved after the interior solution is obtained. The normal velocity perturbation is then found by substituting the acoustic pressure solution into the impedance condition Eq. (9).

In the present work, the solution is stored at the cell centers, rather than the nodal points on the mesh. This approach overcomes the singularity problem that exists along the centerline in the current formulation. As a result of this, the wall conditions are applied between a ghost point inside the wall and the first interior grid point off the wall. This in turn requires interpolation of the data on the wall points. Third-order interpolation is used to this effect. Extrapolations of tangential contravariant velocities and density are also done to third-order accuracy.

III. Grid System and Parallelization

Conformal mapping is used to generate the meshes used. Such a mesh is shown in Fig. 1 with its domains for the parallel computing approach of the present method. Each domain is assigned to a different processor that is on a network for distributed computing. Boundary data are exchanged across the interface between two neighboring subdomains, that is, communication among the processors, and message passing interface protocol is used for parallelization. In general, a three-dimensional domain decomposition is used such that the ratio of the surface work to the volume work is minimum.

IV. Discussion of Simulations

Axisymmetric and three-dimensional computations pertaining to the JT15D inlet geometry are presented. Particularly, forward radiation of the (0, 0) + (0, 1), and spinning (6, 0) and (13, 0) modes is considered at different operating conditions. Axisymmetric computations are carried out for the (0, 0) + (0, 1) modes, whereas full three-dimensional computations are performed for the spinning modes. A single spinning mode represents periodic waves in the azimuthal direction. Therefore, for such cases it is sufficient to consider only one pressure lobe with periodic boundary conditions to reduce the computation time. The inlet centerbody is omitted in computations of the (0, 0) + (0, 1) and (6, 0) modes but retained in computation of the (13, 0) mode.

Calculations employ only fourth-order artificial dissipation to provide the necessary background dissipation with minimal effects on the physical waves. Local time stepping is used for steady-state solutions (mean flow), but for acoustic calculations, the time-step size Δt is determined based on the BPF such that Δt is within the stability bounds of the scheme. Far-field sound is determined using a moving surface Kirchhoff's formula (see Ref. 12). The details of the Kirchhoff algorithm are given by Özyörük and Long.[2] The acoustic treatment panel used in computations of the plane wave modes and the spinning (6, 0) mode is that in Ref. 7. The impedance values of this liner and that used for the spinning (13, 0) mode are given in Table 1 for the frequencies considered in the paper.

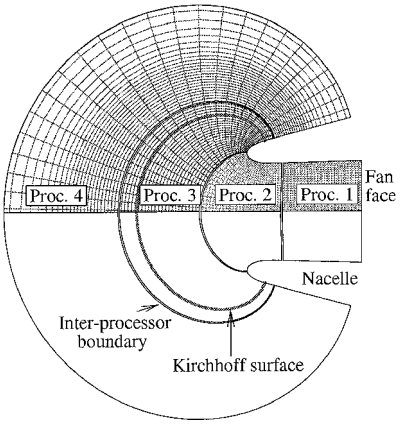

Fig. 1 Computational mesh and its decomposition for distributed parallel computing (every other grid line shown).

A. Radiation of (0, 0) + (0, 1) Modes Without Mass Flow

The first case involves tonal radiation of the plane wave modes (0, 0) and (0, 1) combined up to the fourth harmonic of the BPF forming a multifrequency source. A 180-deg phase difference is introduced between the (0, 0) and (0, 1) modes of each harmonic, and the total acoustic pressure amplitude for each pair is selected to carry a sound pressure level of 120 dB at the rotor blade tips. The BPF is chosen as 0.5 kHz so that the highest harmonic (for which the frequency is 2 kHz) does not exceed the resolution requirement of the mesh. At these conditions, only the (0, 1) mode at the BPF is naturally cut off. The grid has 192 × 48 points along the inlet surface and in the normal direction to it, respectively. Figure 1 shows the mesh with every other grid line deleted for clarity. The grid is divided into four subdomains for parallel processing. The Kirchhoff surface location is also illustrated in Fig. 1. In the important region, from the fan face to the Kirchhoff surface, the number of grid points per wavelength does not fall below 16 for the 4 BPF waves. This grid resolution is sufficient for propagating the waves numerically without significant numerical error buildup.[2] The time-step size is taken as 1/1024 BPF. Three different liner locations are chosen for comparison purposes, with a constant material length of 0.21 m.

The liner locations are shown in Figs. 2a and 2b along with the computed acoustic pressure contours from excitation at the fan face using these modes. No mass flow exists. The effect of the acoustic treatment is clear from Figs. 2a and 2b. It is evident that there is strong focusing of the waves toward the centerline. When compared with the hard-wall case, the generation of some additional modes over the liner is observed, especially for liner position 1. These modes propagate both in upstream and downstream directions. The fan-face conditions yielded only minor reflections, which did not extend back out to the Kirchhoff surface location shown in Fig. 1. This was observed for each liner location considered, when the acoustic pressure contours at different wave periods were compared.

Table 1 Liner impedance

Frequency, kHz	$Z/\rho_0 c_0$
0.5	$0.406 - 1.587i$
1.0	$0.476 + 0.113i$
1.5	$1.078 + 1.638i$
2.0	$5.009 - 0.276i$
2.1	$4.008 - 1.601i$
3.15	$0.638 + 0.500i$
3.15	$1.136 + 0.500i$

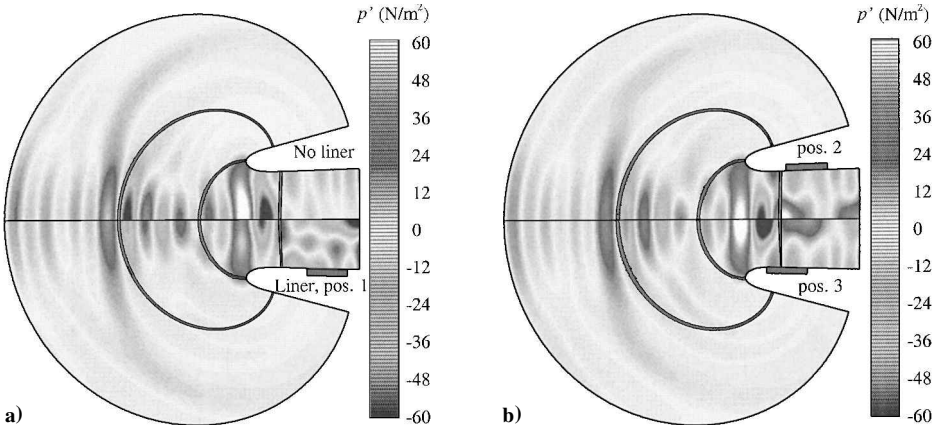

Fig. 2 Alteration of acoustic field by liner: a) upper half without liner and lower half with liner at position 1 and b) upper and lower halves with liner at positions 2 and 3, respectively.

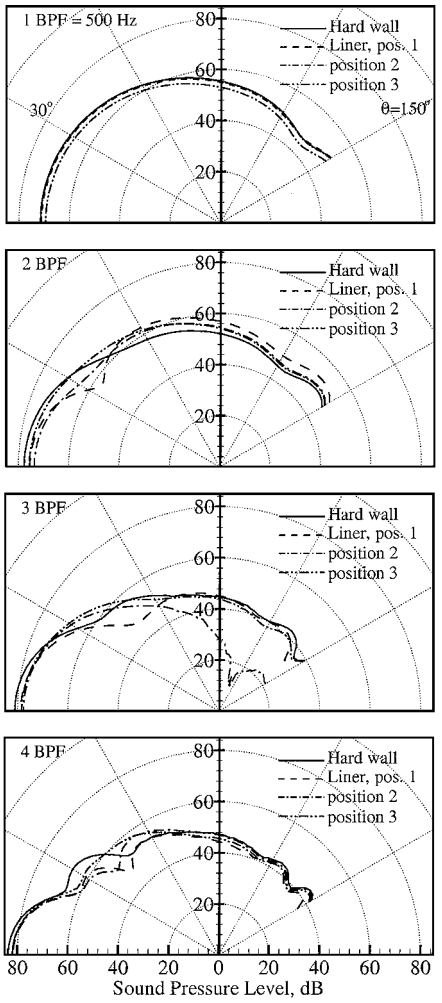

Fig. 3 Effect of liner placement on far-field sound levels and directivity; source (0, 0) and (0, 1) modes with 180-deg phase difference combined at 1 BPF (0.5 kHz), 2 BPF, 3 BPF, and 4 BPF without mass flow.

The Kirchhoff surface integration results for the far-field sound are given in Fig. 3 for each harmonic of the fundamental frequency, which were separated by a fast Fourier transform. Kirchhoff integrations were performed at every fourth time step of the R–K integration for a 50-m radius arc from the inlet mouth. Because the (0, 1) mode is cut off at 1 BPF, sound pressure level (SPL) curves do not exhibit any wave reinforcements or cancellations at far-field points at this low frequency. It is evident from Fig. 3 that liner position 3 is the best location for absorbing noise at this particular frequency, though the total attenuation is not significant compared to that for the 2 BPF components. Although all liner locations yielded some reduction in SPL in a region up to 40 deg from the inlet axis, there is an increase in SPL between 40 and 150 deg at 2 BPF. As the frequency increases, more lobes appear. Liner position 2 yielded significant attenuation for the 3 BPF components between 60 and 150 deg, although the other locations did not. Liner position 1 appears to be the best in overall attenuation pattern at 3 BPF. The 4 BPF components are also absorbed significantly with this position of the liner.

B. Radiation of (0, 0) + (0, 1) Modes with Flow

In this section, the ability of the code is demonstrated with mass flow. Again the (0, 0) and (0, 1) modes are selected for excitation, but at a BPF of 2.0 kHz. Introducing additional frequencies caused stability problems due to the sudden jump in the impedance at the junctions of the liner and hard walls, similar to those discussed in detail in Refs. 7 and 8. It was shown in Ref. 8 that this type of instability could be removed using a sheared background flow. The freestream Mach number and the MFR are arbitrarily taken to be 0.204 and 15 kg/s, respectively. A mean-flow calculation is carried out first, until the residual is driven about 12 orders of magnitude down. Then acoustic computations are started from the steady-state solution, with $\Delta t = 1/512$ BPF. At BPF = 2.0 kHz, the cutoff ratios for the (0, 0) and (0, 1) modes are ∞ and 2.6, respectively. The total amplitude of these modes is set to a fluctuation level of 110 dB at the rotor tip. The same mesh as the preceding case is used, and the liner is at location 2 with the same length.

The mean pressure contours are shown in the lower half of Fig. 4a, whereas the acoustic pressure contours with the liner are shown in the upper half for two different wave cycles. It is evident from the acoustic pressure contours that the wave field is perfectly harmonic, indicating no reflections. The effect of the liner on the acoustic field is demonstrated in Fig. 4b. It is clear that the liner causes partial absorption and redistribution of acoustic energy. The resulting far-field SPL from the Kirchhoff integrations is shown in Fig. 5. The liner caused about a 3-dB reduction in SPL in the upstream direction while it reached the peak value in a direction about 35 deg from the inlet axis. Note, however, that the liner causes an increase in the noise level between approximately 45 and 90 deg from the inlet axis. The reason for this is the generation of additional modes by the liner, causing new reinforcement and cancellation patterns of the waves.

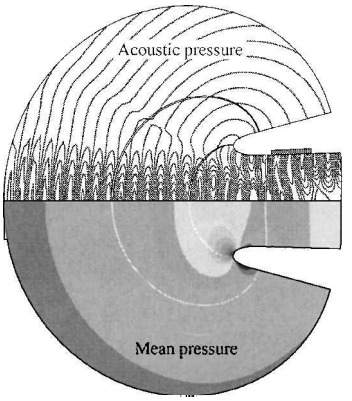

Fig. 4a Acoustic pressure contours showing periodicity of solution with liner present (upper half) (contours of p_a at ——, t = 30 T and · · · · ·, t = 38 T), and mean pressure contours (lower half).

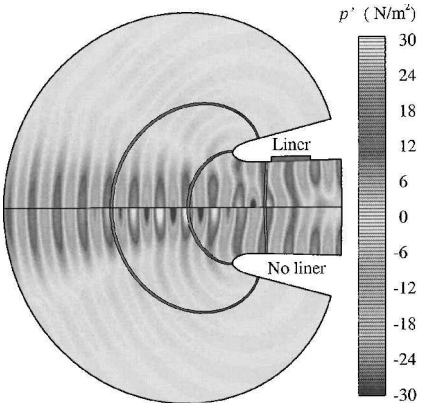

Fig. 4b Effect of liner on acoustic field; source (0, 0) + (0, 1) modes with 180-deg phase difference at M_∞ = 0.204, MFR = 15 kg/s, and BPF = 2 kHz.

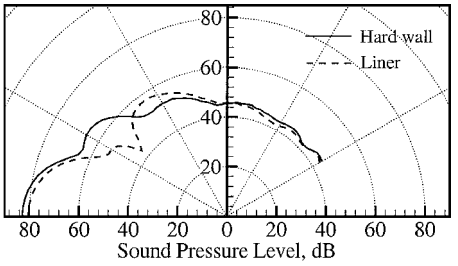

Fig. 5 Effect of liner on far-field sound levels and directivity; source (0, 0) + (0, 1) modes with 180-deg phase difference at M_∞ = 0.204, MFR = 15 kg/s, and BPF = 2 kHz.

C. Radiation of Spinning (6, 0) Mode with Flow

We now consider the (6, 0) spinning mode, resulting from a choice of 21 rotor blades and 15 stator vanes. The same flow conditions as the preceding section apply to this case. The rotor speed is assumed to be 6000 rpm. This gives rise to the (6, 0) spinning mode at a BPF of 2.1 kHz, with a cutoff ratio of 1.3. The wave amplitude is set to about 16 Pa at the rotor tip. The time step size Δt is fixed to 1/768 BPF. Computations use the same grid as the preceding cases, except 16 additional grid points per lobe are introduced in the azimuthal direction.

Figure 6 shows the computed acoustic wave patterns at the fan face and on the inlet cowl both for the hard-wall and soft-wall cases. It is clear from the comparison of the images that the liner causes a reduction in the radiated noise. This is better demonstrated in Fig. 7, where instantaneous acoustic pressure variations are shown along the inside surface for a hard-walled cylindrical duct using the exact solution (solid curve), for the hard-walled JT15D inlet (dashed curve), and for the lined JT15D inlet (dashed–dotted curve). A comparison of the exact circular duct solution and the hard-walled JT15D solution indicates that the code captured the spinning pressure wave pattern well. The small phase and amplitude differences between the two are caused by the nonuniform cross sections of the JT15D inlet. It is also evident from Fig. 7 that the liner causes significant attenuation of the pressure wave as it propagates from right to left. This is quantified in Fig. 8 with the far-field SPL calculated again on a 50-m arc from the inlet mouth using the Kirchhoff surface shown in Fig. 1. The most radiation occurs in a direction about 50 deg from the inlet axis. The impedance condition given by Eq. (3) was used with and without the convected terms for comparison purposes. In both cases the liner did not render a significant shift in the main lobe direction, but it reduced the noise level by approximately 10 dB with the convected term present and about 8 dB without it. The main reason for such a relatively higher attenuation compared to those for the plane wave modes is that a spinning mode traverses longer distances over the liner element. The distance a spinning mode traverses before it radiates to the far field depends on the cutoff ratio of the mode.

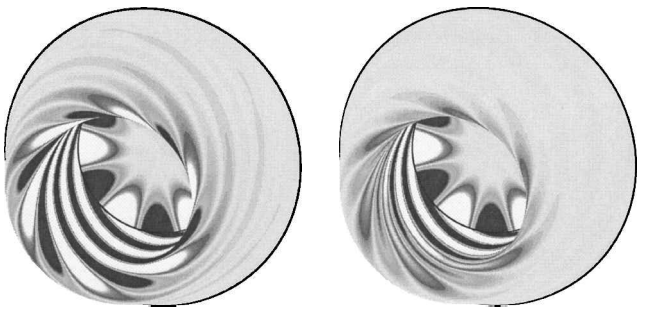

Without liner **With liner**

Fig. 6 Acoustic pressure contours at fan face and on inlet wall; acoustic source (6, 0) mode at M_∞ = 0.204, MFR = 15 kg/s, and BPF = 2.1 kHz.

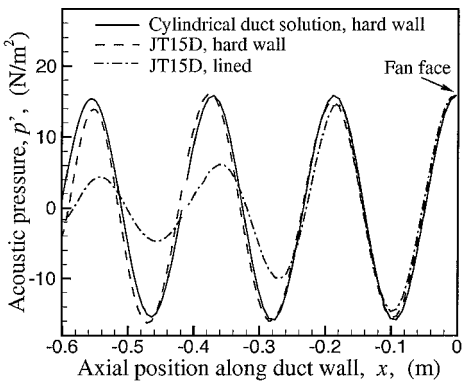

Fig. 7 Instantaneous acoustic pressure at axial positions along inside surface of inlet wall; acoustic source (6, 0) mode at M_∞ = 0.204, MFR = 15 kg/s, and BPF = 2.1 kHz.

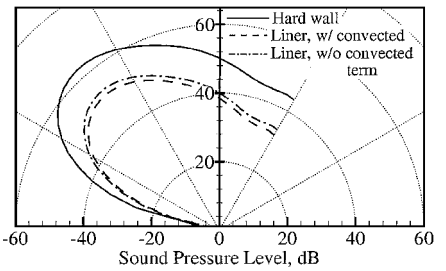

Fig. 8 Effect of liner on far-field sound; acoustic source (6, 0) mode at M_∞ = 0.204, MFR = 15 kg/s, and BPF = 2.1 kHz.

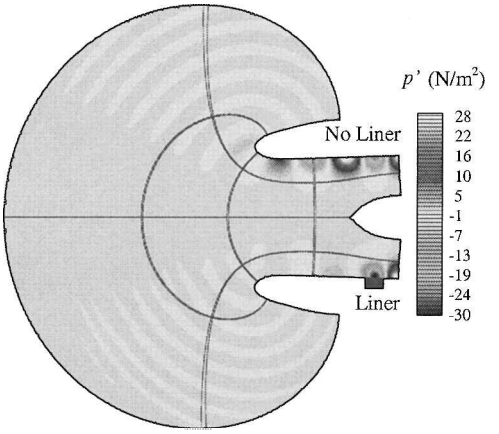

Fig. 9 Effect of liner on sound radiation; source (13, 0) mode at M_∞ = 0, MFR = 11.9 kg/s, BPF = 3.15 kHz, and $Z/\rho_0 c_0 = 1.136 + 0.5i$.

D. Radiation of Spinning (13, 0) Mode with Flow

Radiation of the (13, 0) mode is considered with and without a liner at the static test conditions of Heidelberg et al.,[13] and the results are compared with their experimental data. Although they employed a constant radius duct with a thick inlet lip, the inner wall contour of the actual JT15D inlet[14] is used in the present study. However, the outer wall contour is slightly modified. The centerbody is also included in the simulations. The liner is placed 0.126 m upstream from the fan face and has a length of 0.08 m. Two different normalized impedance values, $0.638 + 0.5i$ and $1.136 + 0.5i$, are tested at a freestream Mach number of zero and MFR of 11.9 kg/s. At these conditions, flow develops through the inlet with the mean Mach number reaching 0.147 at the fan, which matches the experimental conditions.[13] The BPF is set to 3150 Hz, and the mode cutoff ratio at this frequency is 1.05. Computations employ a grid of $241 \times 57 \times 18$ points per circumferential lobe. This grid provides a resolution of about 16 points per wavelength in the flow region enclosed by the Kirchhoff surface, which is located at a position similar to the preceding cases. This grid resolution is sufficient not to allow significant numerical error accumulation while the acoustic waves are propagating through this region. Computations are carried out on eight processors simultaneously.

The mean flowfield was obtained first, which drove the residual about 12.4 orders of magnitude down. Then the acoustic source was turned on with an SPL of 120 dB at the inlet wall. Resulting acoustic pressure contours are shown in Fig. 9. The upper half of Fig. 9 shows the radiation pattern for the hard-walled duct and the lower half for the lined inlet with an impedance value of $0.638 + 0.5i$. The effect of the liner on the radiation of the (13, 0) mode is demonstrated with the far-field directivity plots in Fig. 10, where the symbols are the experimental data of Heidelberg et al.[13] Although the hard-wall case yielded a very good comparison, the attenuation rates with the liner were underpredicted. Numerical experimentation showed that the additional modes created by the liner propagate downstream, and for this particular mode, the present fan-face condition does not allow these relatively strong waves pass the boundary properly, which results in some reflections at the given operating conditions. These reflections in turn add on the predicted far-field sound. Note

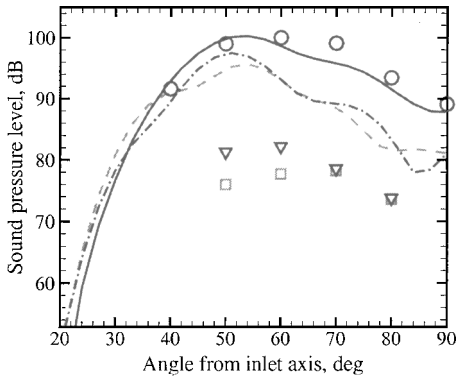

Fig. 10 Far-field sound pressure level; source (13, 0) mode at $M_\infty = 0$, MFR = 11.9 kg/s, BPF = 3.15 kHz. Curves are present simulations: ——, no liner; - - - -, $Z/\rho_0 c_0 = 0.638 + 0.5i$; and –·–, $Z/\rho_0 c_0 = 1.136 + 0.5i$. Symbols are experiment[13]: ○, no liner; □, $Z/\rho_0 c_0 = 0.638 + 0.5i$; and ▽, $Z/\rho_0 c_0 = 1.136 + 0.5i$.

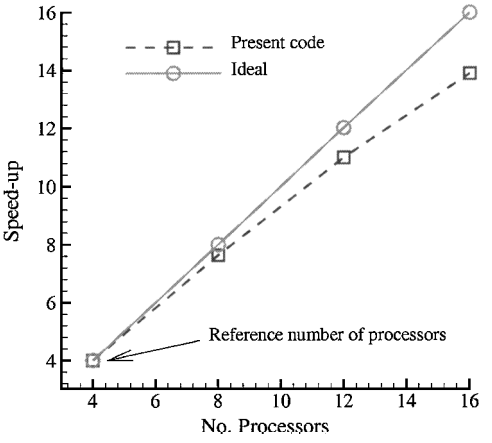

Fig. 11 Parallel code performance.

that such reflections were not observed for the spinning (6, 0) mode discussed in the preceding section. Nevertheless, a general, more robust fan-face boundary treatment is needed to minimize reflections of strong downstream propagating waves.

V. Code Performance

A typical three-dimensional computation for the (13, 0) mode required about 16 h of CPU time on eight 700-MHz Pentium III processors connected with fast ethernet cards. Overall parallel performance of the present code is shown in Fig. 11 for three-dimensional computations with liner. It is clear from Fig. 11 that as the number of processors is increased the parallel performance somewhat diverges from the ideal performance as a result of the increased communication overhead compared to the floating point operations.

VI. Conclusions

A parallel and both spatially and temporally fourth-order-accurate numerical method has been presented for predicting forward radiated noise of ducted fans including the effects of inlet wall acoustic treatment. The method utilized the z transform to imitate the time-domain equivalent of the standard frequency-domain impedance condition. To the author's knowledge, time-domain simulations of a turbofan engine inlet with soft walls have been realized for the first time using this approach. The ability of the algorithm to capture sound attenuation effects of liners was demonstrated by comparing hard- and soft-wall solutions of the JT15D inlet. However, the results presented for the (13, 0) mode showed that the fan-face conditions are vital for accurate far-field predictions, especially when there exist strong downstream traveling waves created by the liner. The present method needs incorporation of a more robust boundary treatment at the fan face.

Acknowledgment

This work was partially supported by the Middle East Technical University through the university research fund AFP.99.03.13.02.

References

[1] Eversman, W., and Roy, I. D., "Ducted Fan Acoustic Radiation Including the Effects of Nonuniform Mean Flow and Acoustic Treatment," AIAA Paper 93-4424, 1993.

[2] Özyörük, Y., and Long, L. N., "Computation of Sound Radiating from Engine Inlets," *AIAA Journal*, Vol. 34, No. 5, 1996, pp. 894–901.

[3] Stanescu, D., Ait-Ali-Yahia, D., Habashi, W. G., and Robichaud, M. P., "Multidomain Spectral Computations of Sound Radiation from Ducted Fans," *AIAA Journal*, Vol. 37, No. 3, 1999, pp. 296–302.

[4] Ahuja, V., Özyörük, Y., and Long, L. N., "Computational Simulations of Fore and Aft Radiation from Ducted Fans," AIAA Paper 2000-1943, June 2000.

[5] Myers, M. K., "On the Acoustic Boundary Condition in the Presence of Flow," *Journal of Sound and Vibration*, Vol. 71, No. 3, 1980, pp. 429–434.

[6] Özyörük, Y., and Long, L. N., "A Time-Domain Implementation of Surface Acoustic Impedance Condition With and Without Flow," *Journal of Computational Acoustics*, Vol. 5, No. 3, 1997, pp. 277–296.

[7] Özyörük, Y., Long, L. N., and Jones, M. G., "Time-Domain Numerical Simulation of a Flow-Impedance Tube," *Journal of Computational Physics*, Vol. 146, No. 1, 1998, pp. 29–57.

[8] Özyörük, Y., and Long, L. N., "Time-Domain Calculation of Sound Propagation in Lined Ducts with Sheared Flows," *AIAA Journal*, Vol. 38, No. 5, 2000, pp. 368–373.

[9] Tam, C. K. W., and Webb, J. C., "Dispersion-Relation-Preserving Finite Difference Schemes for Computational Acoustics," *Journal of Computational Physics*, Vol. 107, Aug. 1993, pp. 262–281.

[10] Bayliss, A., and Turkel, E., "Far Field Boundary Conditions for Compressible Flow," *Journal of Computational Physics*, Vol. 48, Nov. 1982, pp. 182–199.

[11] Tyler, J. M., and Sofrin, T. G., "Axial Flow Compressor Noise Studies," *SAE Transactions*, Vol. 70, 1962, pp. 309–332.

[12] Farassat, F., and Myers, M. K., "Extension of Kirchhoff's Formula for Radiation from Moving Surfaces," *Journal of Sound and Vibration*, Vol. 123, June 1988, pp. 451–460.

[13] Heidelberg, L. J., Rice, L. J., and Homyak, L., "Acoustic Performance of Inlet Suppressors on an Engine Generating a Single Mode," AIAA Paper 81-1965, 1981.

[14] Preisser, J. S., Silcox, R. J., Eversman, W., and Parret, A. V., "A Flight Study of Tone Radiation Patterns Generated by Inlet Rods in a Small Turbofan Engine," AIAA Paper 84-0499, 1984.

P. J. Morris
Associate Editor